ENVIRONMENTAL RESEARCH

PAPER · OPEN ACCESS

Warm Arctic-Cold Eurasia pattern driven by atmospheric blocking in models and observations

To cite this article: Zachary Kaufman et al 2024 Environ. Res.: Climate 3 015006

View the article online for updates and enhancements.

You may also like

- Observed contribution of Barents-Kara sea ice loss to warm Arctic-cold Eurasia anomalies by submonthly processes in winter Yanqin Li, Li Zhang, Bolan Gan et al.

- A surface temperature dipole pattern between Eurasia and North America triggered by the Barents-Kara sea-ice retreat in boreal winter
Yurong Hou, Wenju Cai, David M Holland et al.

- How do intermittency and simultaneous processes obfuscate the Arctic influence on midlatitude winter extreme weather

events?
J E Overland, T J Ballinger, J Cohen et al.

ENVIRONMENTAL RESEARCH

CLIMATE



PAPER

OPEN ACCESS

Warm Arctic-Cold Eurasia pattern driven by atmospheric blocking in models and observations

RECEIVED 25 October 2023



REVISED

- 2 January 2024
- Earth System Science Department, Stanford University, Stanford, CA, United States of America
- ACCEPTED FOR PUBLICATION
- Earth and Planetary Science Department, University of California, Santa Cruz, CA, United States of America
- 16 January 2024
- Ocean Science Department, University of California, Santa Cruz, CA, United States of America Author to whom any correspondence should be addressed.

PUBLISHED

E-mail: zackkauf@stanford.edu

5 February 2024

Keywords: climate dynamics, Arctic sea ice, teleconnections, causal inference

Supplementary material for this article is available online

Original Content from this work may be used under the terms of the Creative Commons

Attribution 4.0 licence. Any further distribution

of this work must maintain attribution to the author(s) and the title of the work, journal citation and DOI.



Abstract

In recent decades, Arctic-amplified warming and sea-ice loss coincided with a prolonged wintertime Eurasian cooling trend. This observed Warm Arctic-Cold Eurasia pattern has occasionally been attributed to sea-ice forced changes in the midlatitude atmospheric circulation, implying an anthropogenic cause. However, comprehensive climate change simulations do not produce Eurasian cooling, instead suggesting a role for unforced atmospheric variability. This study seeks to clarify the source of this model-observation discrepancy by developing a statistical approach that enables direct comparison of Arctic-midlatitude interactions. In both historical simulations and observations, we first identify Ural blocking as the primary causal driver of sea ice, temperature, and circulation anomalies consistent with the Warm Arctic-Cold Eurasia pattern. Next, we quantify distinct transient responses to this Ural blocking, which explain the model-observation discrepancy in historical Eurasian temperature. Observed 1988–2012 Eurasian cooling occurs in response to a pronounced positive trend in Ural sea-level pressure, temporarily masking long-term midlatitude warming. This observed sea-level pressure trend lies at the outer edge of simulated variability in a fully coupled large ensemble, where smaller sea-level pressure trends have little impact on the ensemble mean temperature trend over Eurasia. Accounting for these differences bring observed and simulated trends into remarkable agreement. Finally, we quantify the influence of sea-ice loss on the magnitude of the observed Ural sea-level pressure trend, an effect that is absent in historical simulations. These results illustrate that sea-ice loss and tropospheric variability can both play a role in producing Eurasian cooling. Furthermore, by conducting a direct model-observation comparison, we reveal a key difference in the causal structures characterizing the Warm Arctic-Cold Eurasia Pattern, which will guide ongoing efforts to explain the lack of Eurasian cooling in climate change simulations.

1. Introduction

Arctic sea-ice loss is one of the most dramatic manifestations of global climate change in the observational satellite record (Masson-Delmotte et al 2021), and concurrent Arctic near-surface warming trends have outpaced the global average (Taylor et al 2022). Surprisingly, Arctic-amplified warming and sea-ice loss also coincided with a multi-decade wintertime cooling trend over midlatitude continents, especially between 1988 and 2012 (Cohen et al 2012, Overland et al 2015, Outten et al 2023). While the midlatitude cooling trend has abated in recent years (Blackport and Screen 2020), strong patterns of co-variability between Arctic sea-ice extent and midlatitude surface temperature remain a notable feature of the climate system (Chen et al 2018). This observed covariance has motivated the search for dynamical mechanisms that link Arctic

warming and midlatitude cooling, whereby decreases in sea-ice extent drive changes in extratropical atmospheric circulation.

The clearest regional signature of this Arctic-midlatitude linkage involves negative sea-ice anomalies in the Barents-Kara Sea and cold surface temperature anomalies over Eurasia, which are typically accompanied by anticyclonic circulation anomalies over the Ural Mountains (Luo et al 2016, Mori et al 2019). Together, these metrics represent the Warm Arctic—Cold Eurasia pattern, the primary focus of this study. In the region, a range of relevant mechanisms have been proposed as evidence that sea-ice forced changes in atmospheric circulation cool the midlatitudes. Proposed processes include weakening of the stratospheric polar vortex by vertical wave fluxes over regions of sea-ice loss (Kim et al 2014), weakening of thermal wind by a reduced equator-to-pole temperature gradient (Yao et al 2017), disruptions in tropospheric zonal-mean zonal wind by planetary-scale Rossby waves (Honda et al 2009, Francis and Vavrus 2012, 2015), and the alteration of meridional potential vorticity gradients (Luo et al 2018, 2019, Xie et al 2020). However, atmospheric circulation variability (most notably, Ural blocking) has also been shown to independently drive both Eurasian temperature and sea-ice anomalies, highlighted in both observation-based studies (Sorokina et al 2016, Gong and Luo 2017, Luo et al 2017, Tyrlis et al 2019) and model experiments (Peings 2019, Liu et al 2022). Accordingly, the chain of causality among the co-varying regional anomalies remains unclear, and studies-to-date remain divided on the existence and strength of a forced response to sea-ice loss (Barnes and Screen 2015, Cohen et al 2020).

The source of the Warm Arctic—Cold Eurasia Pattern is further obscured by apparent discrepancies between climate models and observations. Fully coupled climate change simulations generally show weak midlatitude responses to sea-ice loss and are unable to reproduce the observed prolonged period of historical Eurasian cooling (Sun *et al* 2016, Boland *et al* 2017, Ogawa *et al* 2018). This model-observation discrepancy has been attributed to internal climate variability (Blackport and Screen 2021), as well as to systematic underestimates by models of the variability in Eurasian temperatures associated with sea ice loss (Mori *et al* 2019, Smith *et al* 2022). From a probabilistic viewpoint, these explanations need not be mutually exclusive; anthropogenic sea-ice loss and internal variability can both be important factors that affect the likelihood of prolonged Eurasian cooling (Outten *et al* 2023).

Beyond simulations from freely running coupled models, targeted perturbation experiments can be used to isolate midlatitude responses to sea-ice loss. Yet, the results of these experiments are highly dependent on study design, such as the location of prescribed sea-ice loss (i.e. pan-Arctic vs. regional; Nishii *et al* 2011, Screen 2017), inclusion of a dynamic ocean (Deser *et al* 2016), or the vertical resolution of the climate model being used, which may impact stratosphere-troposphere coupling (Sun *et al* 2015). Separating the forced response to Arctic climate change from internal variability also requires simulating many ensemble members, which entails high computational costs (Liang *et al* 2020, Peings *et al* 2021). Meanwhile, observational studies are constrained by the relatively short length of the reliable satellite record, and empirical evaluations of these observations often lack attributions of causality that could be compared with climate model experiments (Liang *et al* 2021).

This study seeks to identify and quantify causal pathways in the Warm Arctic—Cold Eurasia Pattern. To achieve this goal, we use a statistical causal inference method (Runge *et al* 2019), which has enabled robust quantification of two-way Arctic-midlatitude interactions in observational studies (Kretschmer *et al* 2016, Siew *et al* 2020) and allowed for more direct model-observation comparison without targeted perturbation experiments (Galytska *et al* 2023). Building on these recent advances, our study uses causal inference to compare observed linkages with historical simulations in a fully coupled large ensemble, separating forced responses from internal variability. Additionally, causal effect quantification is combined with linear convolution theory—for the first time, as far as we are aware—to isolate the transient climate response to the time history of midlatitude circulation in each data source. By accounting for the distinct time histories of causal drivers, we reveal the dependence of Arctic-midlatitude connections on different mean climate states. Our approach provides a unique data-driven framework for climate teleconnection research and resolves key barriers to scientific understanding of the Warm Arctic—Cold Eurasia pattern.

2. Methods

We quantify Arctic-midlatitude linkages in observations provided by the NASA Global Modeling and Assimilation Office's latest atmospheric reanalysis product, MERRA-2 (Gelaro *et al* 2017), which includes a satellite-derived sea-ice concentration boundary condition from the NOAA OI SST (Reynolds *et al* 2007) and OSTIA (Donlon *et al* 2012) datasets. Observed causal linkages are compared with fully coupled model output from the CESM2 Large Ensemble (CESM2-LE, Rodgers *et al* 2021), which simulates historical climate change in one hundred ensemble members. By applying our investigation across ensemble members, we can analyze forced climate responses (the ensemble mean), internal variability (the ensemble spread), and the degree to

which observed historical trends lie within simulated internal variability. Lastly, we compare MERRA-2 reanalysis with the latest European Center for Medium Range Weather Forecasting (ECMWF) reanalysis, ERA-5 (Hersbach *et al* 2020), ensuring that our results are robust to the choice of observational data source.

2.1. Regional trend assessment

Following Blackport and Screen (2020), our analysis focuses on the 1988–2012 period, known as a pronounced interval of wintertime Eurasian cooling. In section 3.1, linear trends in 1988–2012 winter (DJF) climate are calculated with an ordinary least squares approach for five spatially aggregated climate indices associated with the Warm Arctic–Cold Eurasia pattern: Barents–Kara sea-ice extent $(65^{\circ}-85^{\circ} \text{ N}, 10^{\circ}-90^{\circ} \text{ E})$, Eurasia near-surface air temperature $(T_{2m}, 40^{\circ}-60^{\circ} \text{ N}, 60^{\circ}-120^{\circ} \text{ E})$, Ural sea-level pressure $(55^{\circ}-70^{\circ} \text{ N}, 40^{\circ}-90^{\circ} \text{ E})$, stratospheric polar vortex strength $([u_{10}], 60^{\circ}-80^{\circ} \text{ N})$, and the phase of the North Atlantic Oscillation (NAO). The first four variables follow the regional definitions used in Blackport and Screen (2021) and are shown with black polygons in figure 1. The NAO time series is calculated by projecting sea-level pressure anomalies in each gridcell onto the first empirical orthogonal function mode of December-March sea-level pressure for the $65^{\circ}-85^{\circ} \text{ N}$, $85^{\circ} \text{ W}-60^{\circ} \text{ E}$ domain (Peings 2019). The NAO is a prominent large-scale mode of climate variability in our region of interest, tracking the strength of the sea-level pressure dipole associated with Icelandic Low and the Azores High. For each variable, we test whether trends are significantly different from zero (5% level) using a two-sided t-test.

In section 3.3, trends in Barents–Kara sea ice and Central Eurasian temperature are calculated in a similar manner, using weekly December–March anomalies. Due to differences in the temporal resolution and seasonal range of these time series, the trend magnitudes differ slightly from those referenced in section 3.1 for the same regions.

2.2. PCMCI algorithm

The PCMCI algorithm (Runge *et al* 2019) is applied in section 3.2 to identify robust causal relationships underlying the Warm Arctic—Cold Eurasia Pattern. The algorithm is characterized by a two-step causal discovery procedure: the PC-stable causality test (named after its creators, Peter Spirtes and Clark Glymour; Spirtes *et al* 2000), followed by the Momentary Conditional Independence (MCI) test (Runge *et al* 2019). Section 2.2.1 describes the first step, and section 2.2.2 describes the second step. Statistical significance assessment in PCMCI is described in section 2.2.3. The Tigramite coding and graphics package for PCMCI (https://jakobrunge.github.io/tigramite/) is used to produce the data discussed in section 3.2 and the causal network visualizations in figure 2. Beyond PCMCI, related causal approaches to studying climate teleconnections can be found in Samarasinghe *et al* (2018), McGraw and Barnes (2020), and Kretschmer *et al* (2021).

One hundred distinct causal networks are constructed for each CESM2-LE ensemble member (historical simulations, 1988–2012) and MERRA-2 reanalysis (observations, 1988–2012), using five input time series. Each time series represents one of the spatially aggregated climate indices described in section 2.1. For observations, we apply a bootstrapping procedure (Siew *et al* 2020) that generates one hundred observation-based time series samples to accompany the one hundred CESM2 ensemble members. The bootstrap samples consist of 24 randomly selected years from the reanalysis period (with replacement). Repeating or removing years from the 1988–2012 period demonstrates which observed causal interactions are intermittent based on their sensitivity to the exact years under consideration. Before input to PCMCI, daily time series variables are linearly detrended and standardized by subtracting the mean and dividing by the standard deviation for each day in the annual cycle. Then, the daily anomalies are downsampled to weekly averages. This high temporal resolution leads to a large sample size, where significant relationships are often associated with small correlation coefficients, as will be shown in section 3.2.

2.2.1. PC-stable

PC-stable identifies a set of potential causal drivers for each variable, x, in the causal network using a series of iterative correlation calculations. In iteration one, every possible time-lagged linear autocorrelation and cross-correlation, from $\tau=1$ to $\tau=\tau_{\rm max}$ (12 weeks), is calculated as:

$$\rho\left(X_i(t-\tau), X_i(t)\right) \tag{1}$$

where ρ is the Pearson correlation coefficient, τ is a time lag (weeks), and $X_i(t-\tau)$ are lagged time series with a potential causal influence on $X_j(t)$. Contemporaneous links are not considered. If the value of ρ is found to be not significantly different from zero, $X_i(t-\tau)$ is eliminated from the set of potential causal drivers of $X_j(t)$. In iteration two, the correlations are re-calculated for the remaining potential drivers as:

$$\rho(X_i(t-\tau), X_i(t))|Z_1) \tag{2}$$

where $Z_1 \neq X_i(t-\tau)$ is the auto or cross-link with the strongest unconditional correlation with $X_j(t)$ in equation (1). The vertical line in equation (2) denotes removing the linear influence of Z_1 from both $X_i(t-\tau)$ and $X_j(t)$ and testing the correlation between their residuals. If Z_1 makes the formerly significant link insignificant, the two variables are said to be conditionally independent, and the link is subsequently removed. This process is repeated over n iterations by adding an increasingly stringent number of conditions, Z_2, Z_3, \ldots, Z_n to the partial correlation tests until no more links can be removed. The PC-algorithm finishes when it converges to a final set of significant links for each variable, which are defined as the 'parents' of each variable: $\mathbf{P}(X_j(t))$.

2.2.2. MCI

In the second step of the PCMCI algorithm, the MCI test, the full set of lagged autocorrelations and cross-correlations is calculated a final time, using each variable's parents identified in step one as a single conditioning set:

$$\rho\left(X_i(t-\tau), X_i(t)|\hat{\mathbf{P}}\left(X_i(t)\right), \mathbf{P}\left(X_i(t-\tau)\right)\right) \tag{3}$$

where $\hat{\mathbf{P}}(X_j(t))$ are the parents of $X_j(t)$, excluding $X_i(t-\tau)$, and $\mathbf{P}(X_i(t-\tau))$ are the parents of $X_i(t-\tau)$. The final set of significant links identified in equation (3) are considered the causes of $X_j(t)$, shown for our system of interest in figure 2. This designation is based on the causal Markov condition, which states that X_j is independent of all network variables, except X_j 's effects, when conditioned on the causes of X_j (Spirtes *et al* 2000).

2.2.3. Significance

When assessing linear partial correlation strength (e.g. ρ in equations (1)–(3)), we apply a statistical significance threshold, α , to define the range of acceptable p-values for rejecting the null hypothesis of conditional independence. For our test statistic, α thus represents the probability of a Type 1 error, or the expected rate of false positives. However, iterative causal discovery procedures, such as PC-stable, consist of repetitive testing, which may affect the rate of false positives. In numerical validations of PC-stable, for instance, combined false positive rates are typically much lower than those expected from individual significance tests (Runge 2018). The two-step approach of PCMCI serves to address this repetitive testing issue.

First, PC-stable is conducted for a range of large significance thresholds, where hyperparameter $\alpha = [0.1,0.2,0.3,0.4]$. The significant links identified for each value of α are used to estimate linear lagged regression models, which are compared using the Akaike Information Criterion (AIC). The choice of α associated with the minimum AIC value defines the parents of each variable in PC-stable, $\mathbf{P}(X_j(t))$ (equations (1) and (2)). In the subsequent MCI tests, the constant conditioning set of equation (3) is able to avoid the sequential testing issue of PC-stable, and α can return to a stricter, robustly defined threshold, with $\alpha = 0.01$ (1%) used in this study. Finally, the p-value of every assessed link in the MCI tests is adjusted using the Hochberg–Benjamini false discovery rate (FDR) control (Benjamini and Hochberg 1995). The adjusted p-values are given by:

$$q = \min\left(P\frac{m}{r}, 1\right) \tag{4}$$

where P is the individual link p-value, m is the number of conditional independence tests applied with equation (3), and r is the ascending-order rank of P among all tests. Ultimately, the significance assessment procedure in PCMCI allows it to achieve high detection power, while simultaneously controlling for the number of false positives (Runge et al 2019).

2.3. Climate response functions

A climate response function can be regarded as a quasi-Green's function, $G(\tau)$, which we use to describe the hypothetical response of temperature and sea ice to a $+1\sigma$ step increase in Ural sea-level pressure at time lag τ (section 3.3). In this study, the calculation of $G(\tau)$ takes place within a causal inference framework, as introduced in Pearl (2013), Runge *et al* (2015), and corresponds to the 'total causal effect' metric described in Kaufman and Feldl (2022).

After uncovering each variable's causal predictors with PCMCI, we quantify causal effects using a vector autoregressive (VAR) model:

$$\mathbf{X}(t) = \sum_{\tau=1}^{\tau_{\text{max}}} \Phi(\tau) \mathbf{X}(t-\tau) + \epsilon_t$$
 (5)

where **X** is a vector of shape (N, t) containing time series for N variables, Φ is a standardized regression coefficient matrix of shape $(N, N, \tau_{\text{max}})$, and ϵ_t is a (N, t) vector of white noise errors. An individual regression coefficient, or link coefficient, $\Phi_{j,i}(\tau)$, indicates the expected change in variable $X_j(t)$ caused by a hypothetical 1σ perturbation in $X_i(t-\tau)$ with all other variables held constant. τ_{max} refers to the time domain over which link coefficients are added. Importantly, $\Phi_{j,i}(\tau) = 0$ unless $X_i(t-\tau)$ causes $X_j(t)$, as determined by PCMCI. This key feature of matrix Φ frees the VAR model from having to fit negligible parameters, thus allowing it to accommodate a large number of variables and time lags.

The causal inference framework also allows us to account for coupled interactions modulating the responses to a step change in a causal network variable. The full set of climate response functions $\mathbf{G}(\tau)$ for a causal network is found by iteratively computing matrix products of the coefficient matrices $\Phi(\tau)$ in equation (5):

$$\mathbf{G}(\tau) = \sum_{s=1}^{\tau} \Phi(s) \mathbf{G}(\tau - s). \tag{6}$$

Note that equation (6) shown above is equivalent to equation 6 in Kaufman and Feldl (2022), except total causal effect $\mathbf{TCE}(\tau)$ is redefined as $\mathbf{G}(\tau)$ to emphasize its mathematical resemblance to Green's functions, which is relevant for the linear convolutions conducted in section 3.3. $\mathbf{G}(\tau)$ can be further decomposed into Green's functions for individual pairs of driver and response variables, which is accomplished by restricting Φ to the specific causal pathways that connect them. In section 3.3, we isolate Green's functions for the Eurasian temperature and Barents–Kara sea-ice response to a Ural sea-level pressure anomaly.

3. Results

3.1. Divergent midlatitude trends

Regional trends associated with the Warm Arctic-Cold Eurasia pattern are shown in figure 1 for boreal winter (DJF), highlighting key similarities and differences between MERRA-2 and the CESM2-LE ensemble mean. Observed and modeled trends both exhibit Arctic sea-ice loss in marginal ice zones (figures 1(a) and (b)) and Arctic-amplified warming below 850 hPa (red contours, figures 1(e) and (f)). The Barents-Kara Sea experiences the largest regional sea-ice loss in both cases, featuring an observed trend of -1.5×10^5 km² per decade and smaller simulated trends of $-0.74 \pm 0.59 \times 10^5$ km² per decade. Beyond Arctic surface climate, large model-observation discrepancies become apparent. Over central Eurasia (solid black polygon, figures 1(c) and (d)), observations feature a significant cooling trend of -1.3 °C per decade (figure 1(c)), whereas simulations feature near-surface warming throughout the Northern Hemisphere (figure 1(d)). Over the Ural mountain region (dashed black polygon, figures 1(c) and (d)) observations feature a prominent positive sea-level pressure trend of 5.0 hPa per decade (green contours, figure 1(c), whereas simulations feature a range of positive and negative sea-level pressure trends, with negligible changes in the ensemble mean $(-0.27 \pm 1.4 \text{ hPa per decade, figure } 1(\text{d})$. In the stratosphere, observations indicate a secondary polar warming peak aloft and a corresponding weakening of the polar vortex, where polar-cap averaged $[u_{10}]$ decreases by -4.7 m s^{-1} per decade (figure 1(e)), though this trend is not statistically significant due to large wintertime variability in stratospheric winds (figure S1). Neither of these features are apparent in the CESM2-LE ensemble mean, where circulation trends associated with the Warm Arctic-Cold Eurasia pattern are absent (figure 1(f)). Figure S2 shows the trends in winter climate in ERA-5 reanalysis, which features the same regional trends seen in MERRA-2.

Notably, the near-surface expression of the Warm Arctic—Cold Eurasia Pattern is able to be captured in some individual CESM2-LE ensemble members (figure S3(a)), where modest Eurasian cooling coincides with positive sea-level pressure trends in a similar spatial pattern to observations. However, the three strongest simulated Ural sea-level pressure trends range from 2.4—3.2 hPa per decade, which is substantially smaller than the observed trend, and Eurasian cooling is also smaller than observed (compare figures 1(c) and S3(a)). Therefore, while CESM2-LE occasionally reproduces aspects of the observed Warm Arctic—Cold Eurasia pattern, the magnitude of observed anomalies are substantially outside the range of simulated variability in the ensemble.

3.2. A robust causal driver of the Warm Arctic-Cold Eurasia pattern

For reanalysis and each CESM2-LE ensemble member, we construct causal networks from the five aforementioned 1988–2012 time series (figures 2 and S4), which highlight drivers of the Warm Arctic–Cold Eurasia pattern. The causal links identified by the PCMCI algorithm are given by the lagged, linear correlations that remain significant after controlling for indirect mediators, common drivers, and autocorrelation (memory). We evaluate relationships amongst detrended anomalies at lags of 1–12 weeks,

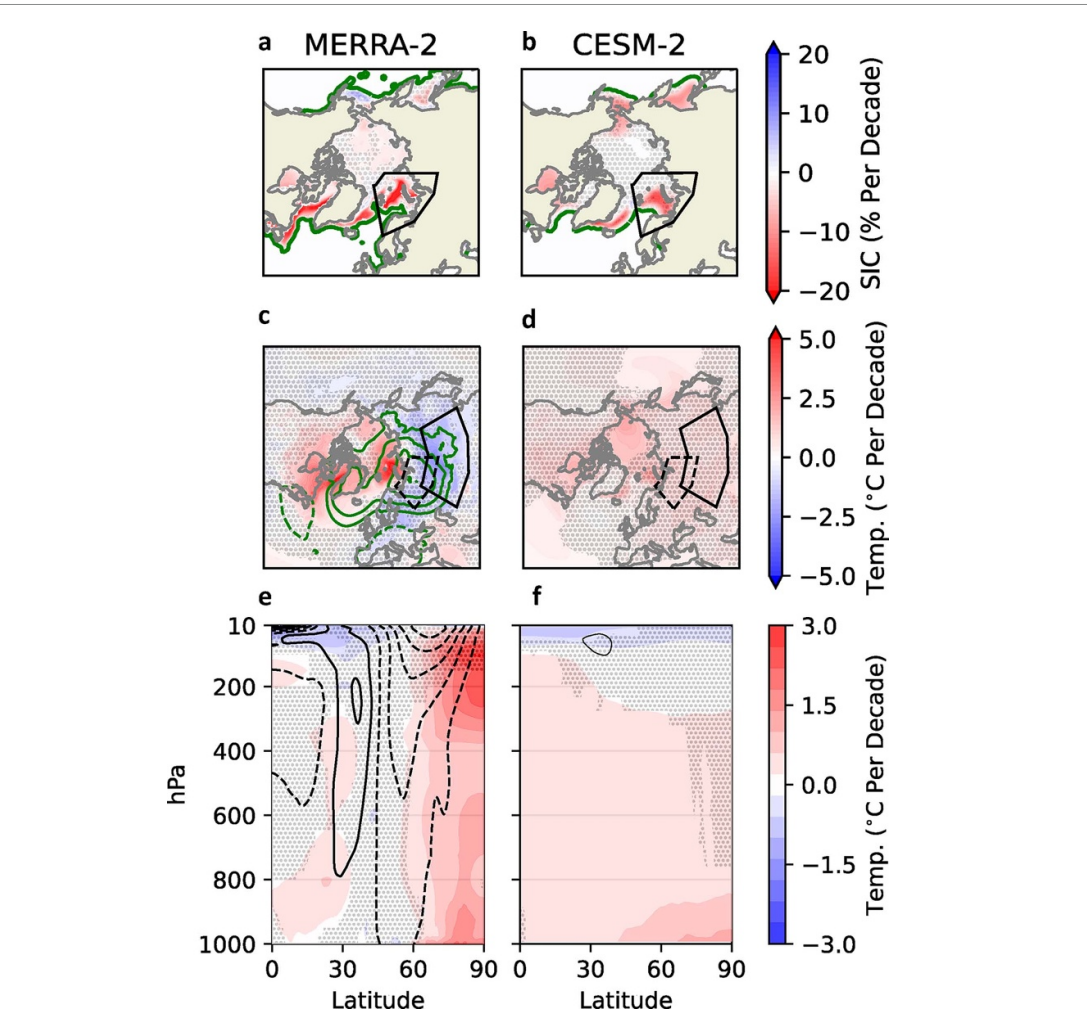


Figure 1. (a) and (b), Trends in Arctic sea-ice concentration (red and blue contours, % per decade) and the climatological DJF sea-ice concentration over the 1988–2012 time period (5% contour, green). (c) and (d), Trends in near-surface air temperature (red and blue contours, $^{\circ}$ C per decade) and sea-level pressure (green contours, hPa per decade), displayed in intervals of 1.5 hPa from −6 to 6 (zero omitted), with dashed and solid contours indicating negative and positive values, respectively. (e) and (f), Vertical profiles of zonal mean trends in temperature (red and blue contours, $^{\circ}$ C per decade) and zonal wind (black contours, m s⁻¹ per decade), displayed in intervals of 1 m s⁻¹ from −7.5 to 7.5, with dashed and solid contours shown as in (c) and (d). The dashed black polygon indicates the Ural blocking region (c) and (d); the solid black polygons indicate the Barents–Kara Sea region (a) and (b) and central Eurasia region (c) and (d). Statistically insignificant trends are indicated with stippling; in (b), (d) and (f), statistical significance is reached when ≥50% of ensemble members have a significant trend. The statistical significance and ensemble spread in spatially aggregated trends are shown in figure S1.

accommodating both the shorter timescale of atmospheric variability and the longer timescale of sea-ice variability. Lastly, we restrict correlation calculations to the months of September–March, encompassing the seasons of maximum Arctic sea-ice loss (early fall) and the active Warm Arctic–Cold Eurasia Pattern (winter). In other words, we evaluate whether December–March anomalies in variable $X_j(t)$ are caused by potential driver $X_i(t-\tau)$ up to 12 weeks in the past, which can include September, October, and November. This temporal masking step accounts for the seasonal dependence of sea-ice variability and any causal effects associated with it.

The causal networks identify two significant causal relationships as remarkably robust in both models and observations, appearing in 99%–100% of MERRA-2 bootstrap samples (figure 2(a)) and CESM2-LE ensemble members (figure 2(b)). Both links are associated with anomalies in Ural sea-level pressure (Node 2.), which predict opposite-signed anomalies in both Barents–Kara sea-ice extent $(2. \rightarrow 1.)$ and central Eurasia T_{2m} (2. \rightarrow 3.). The causal links are strongest at a lag of 1 week, where the average partial correlation coefficient (\bar{r} , link color) between Ural sea-level pressure and Barents–Kara sea-ice is -0.35 in both MERRA-2 and CESM2-LE. The lag-1 partial correlations are similar between Ural sea-level pressure and central Eurasia T_{2m} , with an \bar{r} of -0.33 and -0.32 for MERRA-2 and CESM2-LE, respectively. Interpreted physically, these two robust links indicate that Ural blocking events (positive sea-level pressure anomaly) can drive both sea-ice loss (Warm Arctic, 2. \rightarrow 1.) and midlatitude cooling (Cold Eurasia, 2. \rightarrow 3.) on weekly timescales. In CESM2-LE, the strength of these weekly causal effects does not appear to depend on the

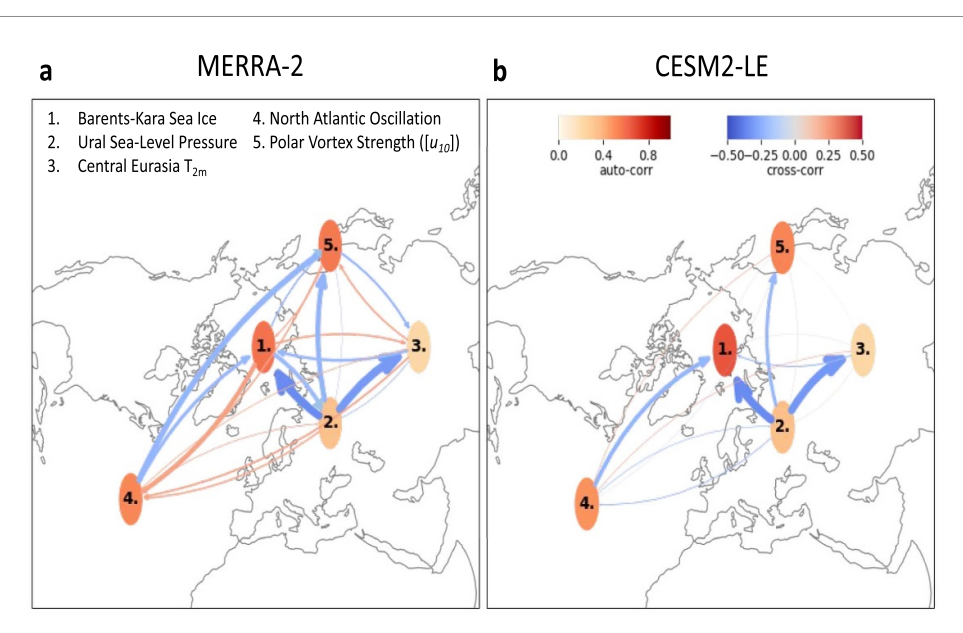


Figure 2. Time-lagged causal links between Barents–Kara Sea ice, Ural sea-level pressure, Central Eurasia 2 m air temperature, NAO Phase, and polar vortex strength ($[\mathbf{u}_{10}]$). Potential causal relationships are evaluated by the PCMCI algorithm over lags of 1–12 weeks for the 1988–2012 period in the months of September–March. Arrows denote the direction and strength of causal links deemed significant at the $\alpha=.01$ level. Arrow thickness indicates the frequency of link detection among the one hundred bootstrap samples from MERRA-2 (a) and one hundred CESM2-LE ensemble members (b), with the thicknest arrows appearing in 99%–100% of samples. Arrow color indicates the average partial correlation coefficient at the time lag with the largest signal; specific lags associated with each link are described in section 3.2. Node color indicates the first-order autocorrelation coefficient associated with each variable.

magnitude of simulated sea-level pressure trends in subsets of ensemble members (figures S3(c) and (d)). Mechanistically, we interpret these causal effects as arising from the impact of anticyclonic blocking circulation on the zonal flow of the midlatitude jet, leading to a localized dipole temperature anomaly, with high-latitude warming on its western flank and midlatitude cooling on its eastern flank. This same mechanism has been detected in prior research of observations (Luo *et al* 2016), as well as in Ural blocking perturbation experiments (Peings 2019).

Interestingly, atmospheric responses to Barents–Kara sea-ice anomalies are comparatively weak and intermittent. In MERRA-2, Ural blocking anomalies are caused by Barents–Kara sea-ice loss $(1. \to 2.)$ at lags of 7–10 weeks $(\bar{r}=-0.21$ at lag-10), but this relationship is only detected in 37% of MERRA-2 bootstrap samples. Barents–Kara sea-ice loss also predicts a negative NAO phase in MERRA-2 $(1. \to 4.)$. This signal is similarly intermittent, being featured in 42% of MERRA-2 bootstrap samples, in agreement with the findings of Siew *et al* (2020). Neither causal link is present in CESM2-LE. Furthermore, while causal networks highlight slackened stratospheric winds as a response to anomalously meridional flow in the troposphere $(2. \to 5.)$, figures 2(a) and (b); $(4. \to 5.)$, figure 2(a)), direct causal links between the polar vortex and Barents–Kara sea-ice extent are nearly non-existent $(1. \to 5.)$. These weak atmospheric responses to sea-ice loss were also found in sensitivity tests (not shown) with monthly time stepping intervals, as well as when changing the averaging region used to define the Barents–Kara Sea.

Our reanalysis results are consistent with prior causal network analyses that identified two-way causality between Barents–Kara sea-ice extent and Ural sea-level pressure at the sub-monthly time scale (Kretschmer *et al* 2016, McGraw and Barnes 2020) and monthly time scale (Galytska *et al* 2023). However, we additionally find that the causal effect of sea-ice loss is intermittent in observations (based on bootstrap resampling) and not captured in an ensemble of historical simulations. This difference is notable given the large discrepancy in Ural sea-level pressure trends in CESM2-LE and MERRA-2 (figures 1(c) and (d); figure S1), which we examine further in the following section. Before proceeding, we conduct a final sensitivity test to verify that the observed causal effect of sea-ice loss (1. \rightarrow 2., figure 2(a)) is not simply an artifact of bootstrap resampling the 1988–2012 time period, since simulating one hundred ensemble members is not equivalent to resampling one real-world realization of the climate system. We find that a MERRA-2 causal network constructed from the original full time series (no resampling) can indeed produce the aforementioned linkage, provided a sufficiently loose significance threshold (α = .05), whereas not a single CESM2-LE ensemble member captures the effect, regardless of the value of α .

Our causal network analysis can thus be summarized as follows. Positive Ural sea-level pressure anomalies (Ural blocking) are a robust atmospheric driver of the Warm Arctic—Cold Eurasia pattern in both

observations (figure 2(a)) and models (figure 2(b)). In observations, a smaller subset of time samples suggest a two-way interaction (figure 2(a)), whereby Ural blocking mediates a Eurasian cooling response to sea-ice loss. These results indicate that Ural blocking variability is the most likely source of the model-observation discrepancy in historical Eurasian cooling (figures 1(c) and 1(c)).

3.3. The transient response to Ural blocking

We next assess how historical trends in Barents–Kara sea ice and Eurasian temperature depend on the time history of Ural blocking. This component of our analysis advances the use of linear convolution theory, whereby the transient response of variable Y to forcing F can be estimated as the convolution of a Green's Function $G(\tau)$ with the time history of the forcing, assuming the response is linear:

$$\hat{Y}(t) \approx \sum_{\tau=1}^{\tau_{\text{max}}} G(\tau) F(t-\tau) \Delta \tau. \tag{7}$$

For our application, Green's Function $G(\tau)$ is the step-response of Y to a one standard deviation perturbation in Ural sea-level pressure at time lag τ (weeks), and $\hat{Y}(t)$ is the transient response to the time history of Ural sea-level pressure $F(t-\tau)$. When derived from model perturbation experiments or lagged linear regressions, $G(\tau)$ has been described as a climate response function (Marshall *et al* 2014, Kostov *et al* 2018, Rye *et al* 2020). Here, we derive $G(\tau)$ from our causal inference framework, where it represents the total causal effect of a hypothetical $+1\sigma$ anomaly in Ural sea-level pressure.

The $G(\tau)$ step responses to Ural sea-level pressure are shown in figure 3 for Eurasia T_{2m} (figure 3(a)) and Barents–Kara sea ice (figure 3(b)). The Eurasian cooling response to a Ural blocking anomaly peaks at $\tau=1$ week, with values of -3.1 °C for MERRA-2 and -2.3 °C for the CESM2-LE ensemble mean, before gradually decaying to zero by $\tau=7$ weeks. Barents–Kara sea ice also decreases in response to Ural blocking, with a $\tau=2$ weeks peak of -0.28×10^5 km² in MERRA-2 and a $\tau=1$ week peak of -0.24×10^5 km² for the CESM2-LE ensemble mean. In both datasets, the sea-ice response persists over a longer time period than the temperature response, consistent with the longer decorrelation length scale of sea-ice anomalies (node color, figure 2). The MERRA-2 responses to a step increase in Ural sea-level pressure are larger than the CESM2-LE ensemble mean, but still well within the ensemble spread, indicating a qualitative similarity (compare black and blue curves, figures 3(a) and (b)).

Despite the similar step responses, observed and simulated Ural sea-level pressure time histories (figure 3(c)) exhibit large differences. Over the entire historical period (1920–2012), there is a 48% chance of observing a positive 24 year trend in wintertime Ural sea-level pressure in CESM2-LE (blue histogram, figure 3(c), but only a 0.14% chance of observing a positive trend as large as the 5.0 hPa per decade trend seen in 1988–2012 observations (vertical dashed line, figure 3(c)), which is the largest 24 year wintertime trend in the satellite era (see figure 1(b), Outten *et al* 2023). This low probability suggests two possibilities: that CESM2 struggles to accurately simulate the observed sea-level pressure trend, or that the observed trend is a rare realization of internal variability. Additionally, even if models and observations have a similar sensitivity to Ural blocking, their transient response to the Ural blocking time histories can be quite different. This difference will become apparent when the Green's functions (figures 3(a) and (b)) are convolved with the Ural blocking time histories (figure 3(c)).

Applying equation (7) to the quantities in figure 3 yields the transient response of Eurasian temperature and Barents–Kara sea ice to the time history of Ural blocking (figure 4). As previously noted, the observed winter trend in Central Eurasia temperature is one of cooling $(-1.0\,^{\circ}\text{C})$ per decade, black curve, figure 4(a)), and the ensemble mean simulated trend is one of warming $(0.80\,^{\circ}\text{C})$ per decade, thick blue curve, figure 4(a)). These divergent midlatitude trends can be reconciled by distinct transient temperature responses to Ural blocking. Specifically, in observations, Eurasia cools strongly, by $-1.9\,^{\circ}\text{C}$ per decade, in response to Ural blocking (black curve, figure 4(b)). By contrast, the wide range of Ural sea-level pressure trends in CESM2-LE (figure 3(c)) produce both negative and positive temperature responses (thin blue curves, figure 4(b)), with a weak positive response in the ensemble mean $(0.13\,^{\circ}\text{C})$ per decade, thick blue curve, figure 4(b)). Once the transient effects of Ural blocking are removed, both observed and simulated Eurasian temperature trends feature a remarkably similar warming signal: $0.89\,$ and $0.67\,^{\circ}\text{C}$ per decade in MERRA-2 and the CESM2-LE ensemble mean, respectively (figure 4(c)). We interpret these warming signals as the trend due to anthropogenic forcing, which, for observations, was masked in figure 4(a) by the cooling associated with an abnormally large Ural sea-level pressure trend.

Unlike Eurasian temperature, models and observations agree that 1988–2012 winter sea-ice retreat occurred in the Barents–Kara sea, as previously shown in figures 1(a) and (b). However, the observed December–March trend in sea-ice extent $(-1.4 \times 10^5 \text{ km}^2 \text{ per decade}, \text{black curve}, \text{figure 4(d)})$ is larger than in the CESM2-LE ensemble mean $(-0.67 \times 10^5 \text{ km}^2 \text{ per decade}, \text{thick blue curve}, \text{figure 4(d)})$. Here too,

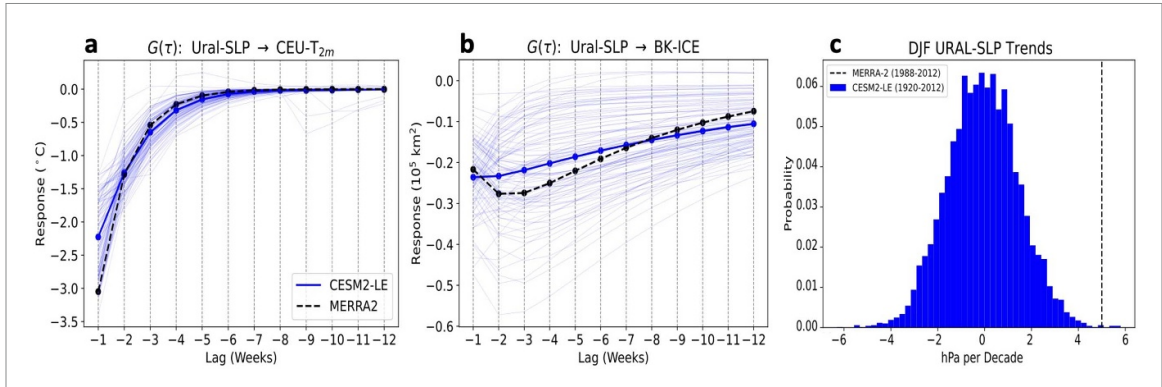


Figure 3. (a) and (b) $G(\tau)$, the estimated response of Central Eurasia T_{2m} (CEU- T_{2m}) and Barents–Kara sea ice (BK-ICE) to a hypothetical $+1\sigma$ step increase in Ural sea-level pressure (URAL-SLP) at lags of 1–12 weeks. Response functions are shown with thin blue lines for one hundred individual CESM2-LE ensemble members, thick blue lines for the CESM2-LE ensemble mean, and dashed black lines for MERRA-2 reanalysis. (c) Probability distribution of 24 year trends in winter (DJF) Ural sea-level pressure (hPa per decade) over the entire historical period in CESM2-LE (1920–2012, blue histogram). The 1988–2012 Ural sea-level pressure trend from MERRA-2 is shown with a dashed vertical line for comparison.

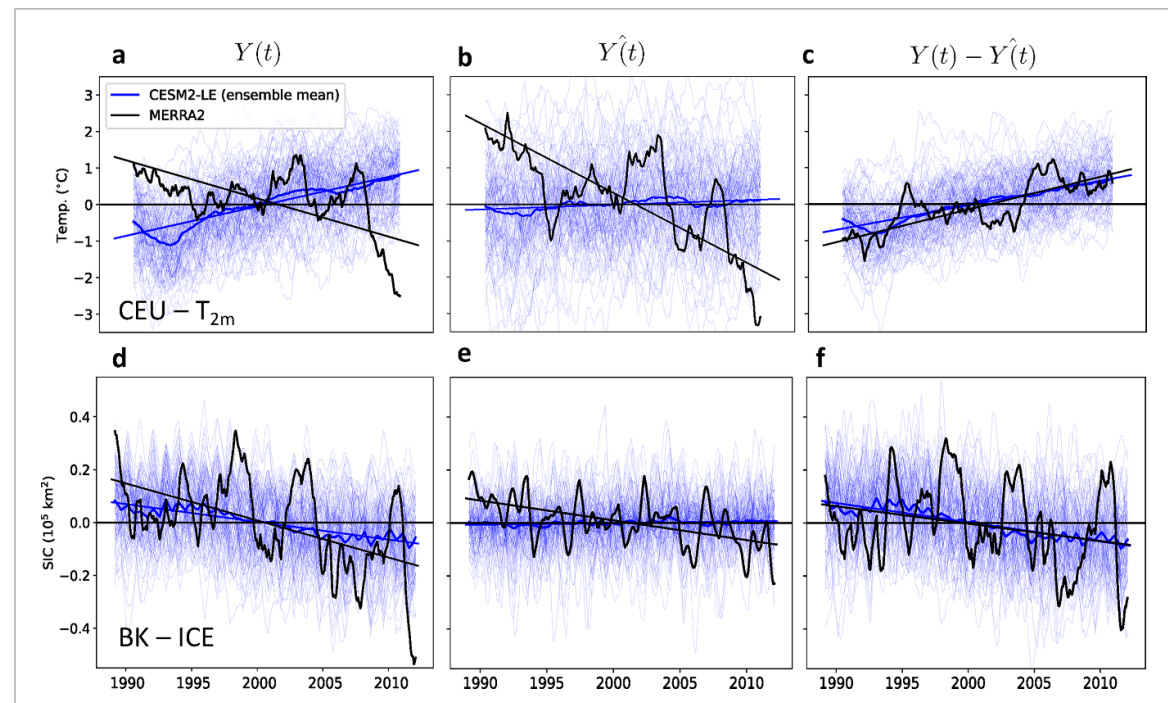


Figure 4. (a)—(c) Time series of Central Eurasia T_{2m} (CEU- T_{2m}) in CESM2-LE (blue) and MERRA-2 (black), shown as weekly December–March anomalies relative to the 1988–2012 climatology. The left column (Y(t), (a)) shows observed and simulated trends, while the middle column (Y(t), (b)) shows the transient response to the time history of Ural sea-level pressure. The right column shows the difference (Y(t)-Y(t), (c)), representing the temperature trends with the effects of Ural blocking variability removed. (d)—(f) The same as (a)—(c), but for 1988–2012 time series of Barents–Kara Sea Ice (BK-ICE). For ease of visualization, a 12 month rolling mean is applied to the weekly temperature anomalies ((a)-(c)) and a 2 month rolling mean is applied to the weekly sea-ice anomalies ((d)-(f)). For all curves, corresponding slope lines are the linear least squares fit to the time series.

accounting for the transient response to Ural blocking helps to bring models and observations into agreement. MERRA-2 features the largest transient response to Ural blocking $(-0.74 \times 10^5 \text{ km}^2 \text{ per decade})$, figure 4(e), which explains half of the observed 1988–2012 winter trend. Unlike MERRA-2, CESM2-LE has a negligible transient response to Ural blocking in the ensemble mean, despite its robust causal relationship with sea-level pressure on weekly timescales (figure 2(b)). The weak sea ice response on longer timescales is due to the absence of sea-level pressure trends in the ensemble mean (figure 1(d)). When the effect of Ural blocking is removed, observed and simulated trends in sea-ice loss are similar $(-0.65 \text{ and } -0.72 \times 10^5 \text{ km}^2 \text{ per decade})$, This similarity implies that the larger sea-ice loss trend in observations (figure 4(d)) can be attributed to the Ural blocking trend (figure 4(e)). In other words, the large positive Ural sea-level pressure trend in MERRA-2 (figure 3(c)) amplified observed 1988–2012 Barents–Kara sea-ice loss.

It is important to note that the transient Eurasian temperature responses to Ural blocking (Y(t), figure 4(b)) are initially calculated assuming that the atmospheric forcing is independent from background

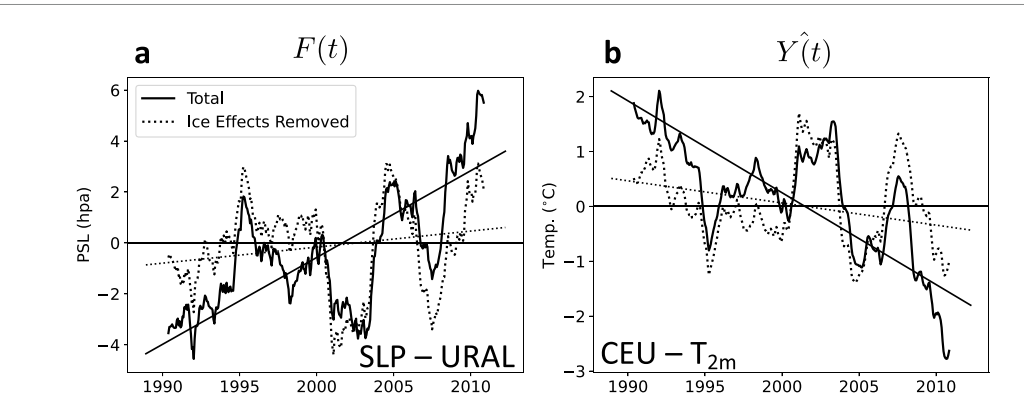


Figure 5. Sea-ice impacts on the transient temperature response to Ural blocking variability in MERRA-2 reanalysis. Time series of Ural sea-level pressure (SLP-URAL, F(t), (a)) and Central Eurasia T_{2m} (CEU- T_{2m} , Y(t), (b)), displayed as anomalies as in figure 4, but for MERRA-2 reanalysis only. The solid curve in (a) (Total) is the observed Ural sea-level pressure trend and the dotted curve is the trend that remains after subtracting the causal effect of 1988–2012 Barents–Kara sea-ice loss. The corresponding curves in (b) are transient responses of Central Eurasia T_{2m} to each forcing time series F(t). Note that the solid curve in (b) is identical to the solid black curve in figure 4(b). For all curves, corresponding slope lines are the linear least squares fit to the time series.

sea-ice trends. This assumption is consistent with the causal links identified in CESM2 historical simulations (figure 2(b)), which only indicate a causal effect of Ural blocking on Barents–Kara sea-ice extent, not vice-versa. However, observations feature bi-directional causality between sea ice and Ural sea-level pressure (figure 2(a)). Accordingly, we further calculate the transient response of Ural sea-level pressure to sea-ice changes in MERRA-2, and subtract it from the sea-level pressure forcing time series, F(t). This adjustment, shown with the dotted curve in figure 5(a), reveals that as much as 80% of the observed Ural sea-level pressure trend is explained by the causal effect of sea-ice loss, which is only found in observations. Therefore, even though the observed causal effect of sea-ice loss on Ural sea-level pressure anomalies is intermittent on weekly timescales (figure 2(a)), the cumulative impact of sea-ice loss on the overall 1988–2012 trends can still be substantial (figure 5). The transient Eurasian temperature response to Ural sea-level pressure in MERRA-2 can also be calculated for both the cooling response to the total trend (solid black curve, figures 4(b) and 5(b)) and the smaller cooling response to the forcing independent of sea-ice changes (dotted curve, figure 5(b)). Comparing the two curves shows that the majority of the total cooling response in MERRA-2 is explained by the indirect effect of sea-ice loss. The smaller, remaining cooling that is independent of sea-ice loss (-.40 °C per decade) is within the ensemble spread of simulated CESM2-LE responses to Ural sea-level pressure (.13 \pm .58 °C per decade, blue curves, figure 4(b)) and thus consistent with internal variability.

4. Summary and discussion

We use a causal inference algorithm to identify a common atmospheric driver of the Warm Arctic—Cold Eurasia Pattern: Both Barents—Kara sea-ice loss and Central Eurasian cooling are caused by positive anomalies in Ural sea-level pressure on weekly timescales. Observed sea-ice loss itself also intermittently affects Ural sea-level pressure (a two-way interaction), but the signal associated with this causal pathway is absent in a set of fully coupled large ensemble simulations. Second, we show that the observed positive trend in Ural sea-level pressure was larger than any of the simulated realizations between 1988 and 2012, lying outside the distribution of simulated variability. The transient response to this Ural blocking trend produced a midlatitude cooling tendency that temporarily masked the long-term warming trend, whilst simultaneously amplifying the rate of anthropogenic sea-ice loss. These results highlight the importance of both anthropogenic sea-ice loss and atmospheric variability for assessing the likelihood of opposing temperature trends in the Arctic and midlatitudes.

While we consider our analysis and findings to be robust, there are potential uncertainties arising from statistical choices and assumptions that should be acknowledged. First, our analysis focuses on the 1988–2012 time period, when particularly large Eurasian cooling was observed. This approach has been used in prior studies (Cohen *et al* 2012, Overland *et al* 2015, Outten *et al* 2023), but caution should still be used when extrapolating our conclusions to different time periods. Second, our study uses a single climate model, the CESM2 large ensemble, even though the strength of Arctic-midlatitude connections likely varies across coupled models (Smith *et al* 2022). Despite this caveat, our use of a large ensemble offers its own advantage of enabling the separation of forced responses from internal variability, as well as elucidating the threshold sea-level pressure trend required to produce multi-decadal Eurasian cooling. Finally, the results of causal

inference analysis can be sensitive to the choice of the variables considered in the causal network. For instance, the causal links connecting sea-ice extent and the NAO could be the result of a remote common driver that is beyond the scope of our analysis, such as the tropical forcing mechanism highlighted in Warner *et al* (2020). Nonetheless, if these subjective choices are appropriately accounted for, causal inference still provides useful and unique scientific insights for the key variables of interest.

Our analysis builds upon the growing body of causal inference studies that highlight intermittent, two-way interactions between Barents-Kara sea-ice extent and midlatitude circulation (Kretschmer et al 2016, 2020, Siew et al 2020, Galytska et al 2023). In spite of this intermittency, we identify an atmospheric driver of the Warm Arctic-Cold Eurasia pattern that is robust across climate states in both models and observations. This key role of Ural blocking is consistent with the mechanisms identified in a variety of targeted model experiments. For instance, Ural blocking anomalies imposed in an otherwise stable climate produce temperature anomalies consistent with the Warm Arctic-Cold Eurasia pattern, as well as a weakened stratospheric polar vortex (Peings 2019). This circulation pattern shapes the midlatitude storm track in a manner that favors moist intrusions into the Barents-Kara sea, where anomalous poleward eddy fluxes lead to sea-ice melt in winter (Woods and Caballero 2016, Luo et al 2017). Meanwhile, Ural blocking simultaneously promotes cold-air outbreaks along its eastern flank, leading to cooling over Eurasia (Luo et al 2016). Our causal networks show that Ural blocking impacts also extend to the upper atmosphere, weakening stratospheric winds, with minimal contributions from sea-ice loss. Unlike the bottom heavy warming signal associated with sea-ice loss, moist energy transport from lower latitudes, including intrusions promoted by Ural blocking, tend to cause more vertically extensive Arctic warming (Feldl et al 2020, Kaufman and Feldl 2022) and a weakened polar vortex (Cardinale et al 2021). Consistent with this dynamical pathway, Eurasian cooling does occur in model experiments with deep tropospheric warming in the Arctic (He et al 2020, Labe et al 2020).

Though Ural blocking variability is clearly central in driving Warm Arctic—Cold Eurasia Pattern, internal variability may not be the only cause of the observed Eurasian cooling period; we also identify an important role for sea-ice loss in modulating the impacts of Ural blocking in MERRA-2 reanalysis. The mechanism for this secondary effect is not immediately apparent in our causal networks, but a recent study has suggested that low sea-ice conditions result in more persistent polar vortex warming after a Ural blocking event, which feeds back onto atmospheric conditions in the North Atlantic (Peings *et al* 2023). A key priority for future work is to ascertain why this coupling between Barents—Kara sea-ice extent and Ural blocking is not captured in CESM2-LE historical simulations, as demonstrated by our model-observation comparison. One possibility is highlighted by the Polar Amplification Model Intercomparison Project (PAMIP), which found that climate models are systematically biased in their representation of the midlatitude eddy momentum feedback, weakening their simulated circulation response to sea-ice loss (Smith *et al* 2022). We recommend that future research establish the relationship between this eddy momentum feedback bias and the Ural blocking response to sea-ice loss. Our causal analysis will provide an essential roadmap for designing these future analyses, bridging the gap between models and observations.

Data availability statement

Analysis code can be made available by Z S K (zackkauf@stanford.edu) upon request.

All data sets used in this study are publicly available. The CESM2 large ensemble output is provided at www.cesm.ucar.edu/community-projects/lens2/data-sets. ERA5 reanalysis is provided at https://cds.climate.copernicus.eu/#!/home and MERRA-2 reanalysis is provided at https://disc.gsfc.nasa.gov/datasets?project=MERRA-2. Causal networks (figure 2) were constructed using the Tigramite python package, release version 5.0.0.3 (https://github.com/jakobrunge/tigramite/).

Acknowledgment

Support for Z S K was provided by the National Science Foundation Graduate Research Fellowship Program under Grant No. (NSF DGE-1842400). N F was supported by NSF award AGS-1753034, and C B was supported by NSF award AGS-2143550.

ORCID iDs

Zachary Kaufman © https://orcid.org/0000-0001-6734-915X Nicole Feldl © https://orcid.org/0000-0002-2631-1419 Claudie Beaulieu © https://orcid.org/0000-0002-0013-5357

References

Barnes E A and Screen J A 2015 The impact of Arctic warming on the midlatitude jet-stream: can it? has it? will it? Wiley Interdiscip. Rev.: Clim. Change 6 277–86

Benjamini Y and Hochberg Y 1995 Controlling the false discovery rate: a practical and powerful approach to multiple testing *J. R. Stat. Soc.* B 57 289–300

Blackport R and Screen J A 2020 Weakened evidence for mid-latitude impacts of Arctic warming Nat. Clim. Change 10 1065–6

Blackport R and Screen J A 2021 Observed statistical connections overestimate the causal effects of Arctic sea ice changes on midlatitude winter climate *J. Clim.* 34 3021–38

Boland E J, Bracegirdle T J and Shuckburgh E F 2017 Assessment of sea ice-atmosphere links in CMIP5 models *Clim. Dyn.* 49 683–702 Cardinale C J, Rose B E, Lang A L and Donohoe A 2021 Stratospheric and tropospheric flux contributions to the polar cap energy budgets *J. Clim.* 34 4261–78

Chen L, Francis J and Hanna E 2018 The 'Warm-Arctic/Cold-continents' pattern during 1901–2010 *Int. J. Climatol.* 38 5245–54 Cohen J L, Furtado J C, Barlow M A, Alexeev V A and Cherry J E 2012 Arctic warming, increasing snow cover and widespread boreal winter cooling *Environ. Res. Lett.* 7 014007

Cohen J et al 2020 Divergent consensuses on Arctic amplification influence on midlatitude severe winter weather Nat. Clim. Change 10 20–29

Deser C, Sun L, Tomas R A and Screen J 2016 Does ocean coupling matter for the northern extratropical response to projected Arctic sea ice loss? *Geophys. Res. Lett.* 43 2149–57

Donlon C J, Martin M, Stark J, Roberts-Jones J, Fiedler E and Wimmer W 2012 The operational sea surface temperature and sea ice analysis (OSTIA) system *Remote Sens. Environ.* 116 140–58

Feldl N, Po-Chedley S, Singh H K, Hay S and Kushner P J 2020 Sea ice and atmospheric circulation shape the high-latitude lapse rate feedback npj Clim. Atmos. Sci. 3 1–9

Francis J A and Vavrus S J 2012 Evidence linking Arctic amplification to extreme weather in mid-latitudes *Geophys. Res. Lett.* 39 6 Francis J A and Vavrus S J 2015 Evidence for a wavier jet stream in response to rapid Arctic warming *Environ. Res. Lett.* 10 014005

Galytska E, Weigel K, Handorf D, Jaiser R, Köhler R, Runge J and Eyring V 2023 Evaluating causal Arctic-Midlatitude teleconnections in CMIP6 J. Geophys. Res. Atmos. 128 e2022JD037978

Gelaro R *et al* 2017 The modern-era retrospective analysis for research and applications, version 2 (MERRA-2) *J. Clim.* 30 5419–54 Gong T and Luo D 2017 Ural blocking as an amplifier of the Arctic sea ice decline in winter *J. Clim.* 30 2639–54

He S, Xu X, Furevik T and Gao Y 2020 Eurasian cooling linked to the vertical distribution of Arctic warming *Geophys. Res. Lett.* 47 e2020GL087212

Hersbach H et al 2020 The ERA5 global reanalysis Q. J. R. Meteorol Soc. 146 1999-2049

Honda M, Inoue J and Yamane S 2009 Influence of low Arctic sea-ice minima on anomalously cold Eurasian winters *Geophys. Res. Lett.* 36 8

Kaufman Z S and Feldl N 2022 Causes of the Arctic's lower-tropospheric warming structure J. Clim. 35 1983-2002

Kim B M, Son S W, Min S K, Jeong J H, Kim S J, Zhang X, Shim T and Yoon J H 2014 Weakening of the stratospheric polar vortex by Arctic sea-ice loss Nat. Commun. 5 1–8

Kostov Y, Ferreira D, Armour K C and Marshall J 2018 Contributions of greenhouse gas forcing and the Southern Annular Mode to historical Southern Ocean surface temperature trends *Geophys. Res. Lett.* **45** 1086–97

Kretschmer M, Adams S V, Arribas A, Prudden R, Robinson N, Saggioro E and Shepherd T G 2021 Quantifying causal pathways of teleconnections Bull. Am. Meteorol. Soc. 102 E2247–63

Kretschmer M, Coumou D, Donges J F and Runge J 2016 Using causal effect networks to analyze different Arctic drivers of midlatitude winter circulation *J. Clim.* 29 4069–81

Kretschmer M, Zappa G and Shepherd T G 2020 The role of Barents–Kara sea ice loss in projected polar vortex changes Weather Clim. Dyn. 1715–30

Labe Z, Peings Y and Magnusdottir G 2020 Warm Arctic, cold Siberia pattern: role of full Arctic amplification versus sea ice loss alone *Geophys. Res. Lett.* 47 e2020GL088583

Liang Y C et al 2021 Impacts of Arctic sea ice on cold season atmospheric variability and trends estimated from observations and a multimodel large ensemble J. Clim. 34 8419–43

Liang Y et al 2020 Quantification of the Arctic sea ice-driven atmospheric circulation variability in coordinated large ensemble simulations Geophys. Res. Lett. 47 e2019GL085397

Liu Z et al 2022 Atmospheric forcing dominates winter Barents-Kara sea ice variability on interannual to decadal time scales *Proc. Natl Acad. Sci.* 119 e2120770119

Luo B, Luo D, Wu L, Zhong L and Simmonds I 2017 Atmospheric circulation patterns which promote winter Arctic sea ice decline Environ. Res. Lett. 12 054017

Luo D, Chen X, Dai A and Simmonds I 2018 Changes in atmospheric blocking circulations linked with winter Arctic warming: a new perspective J. Clim. 31 7661–78

Luo D, Chen X, Overland J, Simmonds I, Wu Y and Zhang P 2019 Weakened potential vorticity barrier linked to recent winter Arctic sea ice loss and midlatitude cold extremes I. Clim. 32 4235–61

Luo D, Xiao Y, Yao Y, Dai A, Simmonds I and Franzke C L 2016 Impact of Ural blocking on winter warm Arctic—cold Eurasian anomalies. Part I: Blocking-induced amplification *J. Clim.* 29 3925—47

Marshall J, Armour K C, Scott J R, Kostov Y, Hausmann U, Ferreira D, Shepherd T G and Bitz C M 2014 The ocean's role in polar climate change: asymmetric Arctic and Antarctic responses to greenhouse gas and ozone forcing *Phil. Trans. R. Soc.* A 372 20130040

Masson-Delmotte V et al 2021 Climate change 2021: the physical science basis Contribution of Working Group I to the Sixth Assessment Report of the Intergovernmental Panel on Climate Change vol 2 (Cambridge University Press)

McGraw M C and Barnes E A 2020 New insights on subseasonal Arctic-midlatitude causal connections from a regularized regression model *J. Clim.* 33 213–28

Mori M, Kosaka Y, Watanabe M, Nakamura H and Kimoto M 2019 A reconciled estimate of the influence of Arctic sea-ice loss on recent Eurasian cooling *Nat. Clim. Change* 9 123–9

Nishii K, Nakamura H and Orsolini Y J 2011 Geographical dependence observed in blocking high influence on the stratospheric variability through enhancement and suppression of upward planetary-wave propagation *J. Clim.* 24 6408–23

Ogawa F et al 2018 Evaluating impacts of recent Arctic sea ice loss on the Northern Hemisphere winter climate change Geophys. Res. Lett. 45 3255–63

Outten S et al 2023 Reconciling conflicting evidence for the cause of the observed early 21st century Eurasian cooling Weather Clim. Dyn. 4 95–114

Overland J, Francis J A, Hall R, Hanna E, Kim S J and Vihma T 2015 The melting Arctic and midlatitude weather patterns: are they connected? *I. Clim.* 28 7917–32

Pearl J 2013 Linear models: A useful 'microscope' for causal analysis J. Causal Inference 1 155-70

Peings Y 2019 Ural blocking as a driver of early-winter stratospheric warmings Geophys. Res. Lett. 46 5460-8

Peings Y, Davini P and Magnusdottir G 2023 Impact of Ural blocking on early winter climate variability under different Barents-Kara sea ice conditions J. Geophys. Res. Atmos. 128 e2022JD036994

Peings Y, Labe Z M and Magnusdottir G 2021 Are 100 ensemble members enough to capture the remote atmospheric response to +2 °C Arctic sea ice loss? *J. Clim.* 34 3751–69

Reynolds R W, Smith T M, Liu C, Chelton D B, Casey K S and Schlax M G 2007 Daily high-resolution-blended analyses for sea surface temperature *J. Clim.* 20 5473–96

Rodgers K B et al 2021 Ubiquity of human-induced changes in climate variability Earth Syst. Dyn. 12 1393-411

Runge J 2018 Causal network reconstruction from time series: from theoretical assumptions to practical estimation *Chaos* 28 075310 Runge J, Nowack P, Kretschmer M, Flaxman S and Sejdinovic D 2019 Detecting and quantifying causal associations in large nonlinear time series datasets *Sci. Adv.* 5 eaau4996

Runge J, Petoukhov V, Donges J F, Hlinka J, Jajcay N, Vejmelka M, Hartman D, Marwan N, Paluš M and Kurths J 2015 Identifying causal gateways and mediators in complex spatio-temporal systems *Nat. Commun.* 6 8502

Rye C D, Marshall J, Kelley M, Russell G, Nazarenko L S, Kostov Y, Schmidt G A and Hansen J 2020 Antarctic glacial melt as a driver of recent Southern Ocean climate trends *Geophys. Res. Lett.* 47 e2019GL086892

Samarasinghe S, McGraw M, Barnes E and Ebert-Uphoff I 2018 A study of links between the Arctic and the midlatitude jet stream using Granger and Pearl causality *Environmetrics* 30 e2540

Screen J A 2017 Simulated atmospheric response to regional and pan-Arctic sea ice loss J. Clim. 30 3945-62

Siew P Y F, Li C, Sobolowski S P and King M P 2020 Intermittency of Arctic-mid-latitude teleconnections: stratospheric pathway between autumn sea ice and the winter North Atlantic Oscillation Weather Clim. Dyn. 1 261–75

Smith D M *et al* 2022 Robust but weak winter atmospheric circulation response to future Arctic sea ice loss *Nat. Commun.* **13** 727 Sorokina S A, Li C, Wettstein J J and Kvamstø N G 2016 Observed atmospheric coupling between Barents sea ice and the warm-Arctic cold-Siberian anomaly pattern *J. Clim.* **29** 495–511

Spirtes P, Glymour C N and Scheines R 2000 Causation, Prediction and Search (MIT press)

Sun L, Deser C and Tomas R A 2015 Mechanisms of stratospheric and tropospheric circulation response to projected Arctic sea ice loss *J. Clim.* 28 7824–45

Sun L, Perlwitz J and Hoerling M 2016 What caused the recent 'Warm Arctic, Cold Continents' trend pattern in winter temperatures? Geophys. Res. Lett. 43 5345–52

Taylor P C et al 2022 Process drivers, inter-model spread, and the path forward: a review of amplified Arctic warming Front. Earth Sci. 9 758361

Tyrlis E, Manzini E, Bader J, Ukita J, Nakamura H and Matei D 2019 Ural blocking driving extreme Arctic sea ice loss, cold Eurasia and stratospheric vortex weakening in autumn and early winter 2016–2017 J. Geophys. Res. Atmos. 124 11313–29

Warner J, Screen J and Scaife A 2020 Links between Barents-Kara sea ice and the extratropical atmospheric circulation explained by internal variability and tropical forcing *Geophys. Res. Lett.* 47 e2019GL085679

Woods C and Caballero R 2016 The role of moist intrusions in winter Arctic warming and sea ice decline J. Clim. 29 4473-85

Xie Y, Wu G, Liu Y and Huang J 2020 Eurasian cooling linked with Arctic warming: insights from PV dynamics J. Clim. 33 2627-44

Yao Y, Luo L, Dai A, Simmonds I, Yao Y, Luo D, Dai A and Simmonds I 2017 Increased quasi stationarity and persistence of winter Ural blocking and Eurasian extreme cold events in response to Arctic warming. Part I: insights from observational analyses *J. Clim.* 30 3549–68